Dynamic Spar Elements and Discrete Element Methods in Two Dimensions for the Modeling of Soil-Inclusion Problems

Bruno Chareyre[1] and Pascal Villard[2]

Abstract: Discrete element methods (DEMs) provide new numerical means to study the behavior of soil-inclusion systems. In some cases, however, the classic DEM fails to model specific aspects of the inclusions. That is why a model based on spar elements is introduced, designed specifically for inclusions. In this model, the movement of the inclusion is considered as a dynamic process and is computed step by step in the same way as in the DEM. The model can be coupled with a DEM code, thus enabling one to simulate the interaction between an inclusion and a disk assembly. Contact laws at the contacts between disks and spar elements describe the interface constitutive behavior. Finally, the results obtained by simulating a geosynthetic anchorage in two different ways are reported. In the first case the inclusion is represented by disks, while in the last case it is represented by spar elements. The comparison shows that spar elements are much more versatile and can simplify the calibration of the discrete models used to simulate soil-inclusion systems.

DOI: 10.1061/(ASCE)0733-9399(2005)131:7(689)

CE Database subject headings: Anchorage; Composite structures; Discrete elements; Soils; Geosynthetics; Granular materials; Interfaces.

Introduction

In the fields of civil and geotechnical engineering, the construction techniques are getting more and more sophisticated and often include composite systems. Particularly, many techniques associate a granular matrix (soil, concrete) with linear or planar inclusions (geosynthetics, fibers, piles, steel rods). Modeling the mechanical behavior of such systems is generally complex since the geometry and governing mechanisms are strongly discontinuous. Traditional finite-element methods, rooted in the concepts of continuum mechanics, may be unsuited in such cases (Villard et al. 2002). At the same time, significant advances in discrete modeling methods offer some opportunities for the numerical simulation of different types of composite systems (Mohammadi et al. 1998; Hentz et al. 2003). Those methods can be used to simulate soil-inclusion systems with respect to their discontinuous nature.

In Chareyre et al. (2002), soil-geosynthetic systems were simulated using the two-dimensional code *PFC2D* (*PFC2D* 1997). This program models bidimensional assemblies of disks with the distinct element method (DEM). In Chareyre et al. (2002), the geosynthetic inclusion was simulated by a chain of disks, as shown in Fig. 1(a), the strength and stiffness of the geosynthetic in tension being related to the tensile strength and tensile stiffness of the contacts between the disks. Although the results obtained with this approach were valuable, this modeling presents two important limitations. First, a roughness related to the size of the disks is inherent in the model. It implies a very complex constitutive behavior of the interface and prevents the model from applying to even-faced inclusions. Second, the axial strain must remain very small or significant voids would be created at each contact between the disks.

The objective of this paper is to propose a model based on spar elements [Fig. 1(b)], adapted to the specific aspects of inclusions, and then to couple it with a DEM code, which simulates granular matters. The two models will interact with respect to a given interface constitutive behavior. It is expected that this coupling will provide a valid numerical tool for much research on soil-inclusion systems.

In the first part, the most important aspects of the DEM code used will be set out. In the second part, the model proposed for the inclusions will be presented; it is denoted as the DSEM for the dynamic spar element model. Finally, the results obtained by simulating geosynthetic anchorages in soil will be reported. They were obtained by modeling the inclusion with each of the concepts in Fig. 1 to provide a comparison.

Distinct Element Method

In the present study, the soil is modeled using the program *PFC2D*, which is an implementation of the model of Cundall and Strack (1979). This section briefly summarizes the method used in *PFC2D* to calculate contact forces from displacements and to determine the motion of the disks, a more detailed description may be found in *PFC2D* (1997).

[1]Assistant Professor, LTDS, Ecole Centrale de Lyon, 36 Ave. Guy de Collongue, 69134 Ecully, France. E-mail: bruno.chareyre@ec-lyon.fr

[2]Assistant Professor, LIRIGM, Joseph Fourier's Univ. of Sciences, 38041 Grenoble, Cedex 9, France.

Note. Associate Editor: Jin Y. Ooi. Discussion open until December 1, 2005. Separate discussions must be submitted for individual papers. To extend the closing date by one month, a written request must be filed with the ASCE Managing Editor. The manuscript for this paper was submitted for review and possible publication on April 30, 2003; approved on September 16, 2004. This paper is part of the ***Journal of Engineering Mechanics***, Vol. 131, No. 7, July 1, 2005. ©ASCE, ISSN 0733-9399/2005/7-689–698/$25.00.

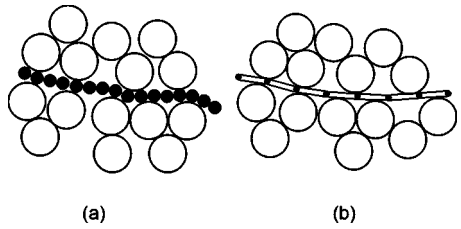

Fig. 1. Two different concepts to model soil-inclusion systems with the distinct element method (DEM): (a) full-DEM modeling or (b) DEM–dynamic spar element model modeling. The disks in white represent the soil.

Contact Model

The contact model relates the relative displacement to the force acting at the contact between two disks. In this study, the contact model consists of a linear stiffness model and a Coulomb-like slip model (Fig. 2). The stiffness model is defined by two parameters: normal stiffness k_n^* and tangential stiffness k_t^*. The normal and the tangential components of the contact force are proportional, respectively, to the overlap between two disks in contact and to the tangential displacement at contact. The tangential component of the contact force is limited in magnitude with respect to the Coulomb-like slip model, with friction angle μ^*.

Motion

The disks interact with each other via contact forces. The method to calculate the displacement from the resultant force and torque acting on a disk is summarized below. The angle of rotation of the disk is denoted as θ_3. $\boldsymbol{y}_i$ represents the position vector of the center of the disk. Newton's second law of motion relates the translational and rotational accelerations to the resultant force and torque, $\boldsymbol{f}_i$ and M_3

$$\ddot{\boldsymbol{y}}_i = \boldsymbol{F}_i/m_D \tag{1}$$

$$\ddot{\theta}_3 = M_3/I_D \tag{2}$$

Here, m_D and I_D denote, respectively, the mass and moment of inertia of the disk. During a simulation, the movement of each disk is traced step-by-step, at time intervals Δt. $\ddot{\mathbf{y}}_i$ and $\ddot{\theta}_3$ are integrated over Δt following an explicit centered finite-difference scheme, as in the set of equations below [Eqs. (3)–(6)]. In the equations, a subscript after a bracket denotes the time step with respect to which the expression is considered.

$$[\dot{\boldsymbol{y}}_i]_{t+\Delta t/2} = [\dot{\boldsymbol{y}}_i]_{t-\Delta t/2} + [\ddot{\boldsymbol{y}}_i]_t \times \Delta t \tag{3}$$

$$[\dot{\theta}_3]_{t+\Delta t/2} = [\dot{\theta}_3]_{t-\Delta t/2} + [\ddot{\theta}_3]_t \times \Delta t \tag{4}$$

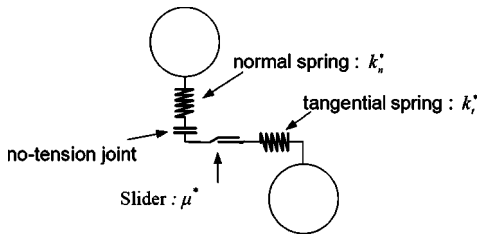

Fig. 2. Contact model

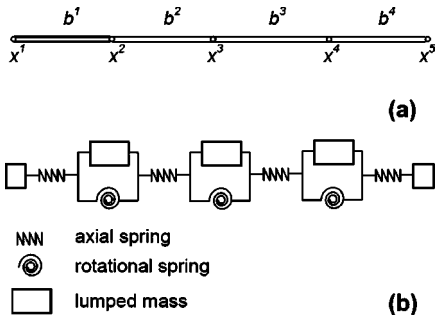

Fig. 3. Notation of (a) the nodes and spar elements and (b) the rheological model for a five-noded inclusion

$$[\boldsymbol{y}_i]_{t+\Delta t} = [\boldsymbol{y}_i]_t + [\dot{\boldsymbol{y}}_i]_{t+\Delta t/2} \times \Delta t \tag{5}$$

$$[\theta_3]_{t+\Delta t} = [\theta_3]_t + [\dot{\theta}_3]_{t+\Delta t/2} \times \Delta t \tag{6}$$

When all positions are calculated for time $t+\Delta t$, contact forces may be calculated for the next calculation cycle.

Setting the value of Δt in Eqs. (3)–(6) and damping the equations of motion are two essential issues of the DEM. For the case of a disk assembly, those aspects are detailed in *PFC2D* (1997) and will not be developed in this paper. However, modeling with dynamic spar elements raises similar questions. The methods proposed below for setting Δt and damping the equations of motion in the DSEM can give an overview of what is done for disks.

Dynamic Spar Element Model

This section is dedicated to the presentation of the dynamic spar element model and the coupling with the DEM code. The DSEM was initially designed specifically for the modeling of geosynthetic sheets, which have generally no bending strength. However, it is believed that the DSEM could equally apply to other types of inclusions. In this perspective, the formulation proposed here can handle problems in which the bending strength has to be considered.

In the DSEM, the motion of the spar elements is determined in the same manner as in the DEM, and the soft contact approach is adopted for the interaction between the disks and the inclusion. Consequently, the DSEM may be viewed as an implementation of the DEM, and the formulation detailed in this section is partly based on the concepts developed in the DEM-related publications of P. A. Cundall. For the sake of simplicity, however, it will be considered in this paper that the DEM and DSEM are two different numerical models. The DSEM's specificities are mainly due to the shape and the deformability of the elements, the type of connexion between them, and the inertial model.

Discretization

The inclusion is represented by a set of spar elements connected by nodes, as in Fig. 3(a). The length of the elements is considered variable, the axial deformation being accounted for by a variation of the distances between the nodes; the flexion of the inclusion is represented by rotations at the nodes; and the flexion of an individual element is not considered. In the next part, the length of the elements will be related to the axial forces, and the rotation at nodes to the bending moments. From the inertial viewpoint, the inclusion is treated as a set of lumped masses coinciding with the

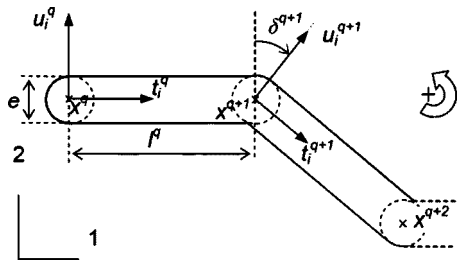

Fig. 4. Geometry and notations

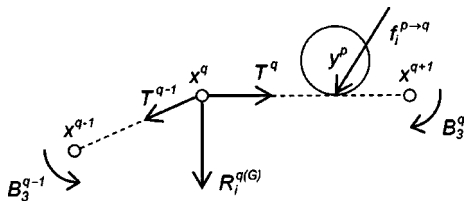

Fig. 5. Types of load participating in the resultant force acting on node x^q

nodes. This rheological model is illustrated in Fig. 3(b). The interaction between the inclusion and the granular matter will be treated with the soft contact approach. It implies that the disks and the spar elements will be allowed to overlap with one another at contact points. Hence it is necessary to consider the thickness e of the spar elements, otherwise two disks could get in contact and overlap with one another across the inclusion. In the case of the flexion at a node, the evenness of the convex side is ensured with a circular arc centered on the node and of radius $e/2$ (see Fig. 4). Following the same principle, the shape of the ends of the inclusion is defined by semicircles.

Some notations used in the rest of the paper are defined in Figs. 3 and 4. An inclusion is represented by N^b elements. The elements are denoted as $\{b^1,\ldots,b^{N^b}\}$, the nodes as $\{x^1,\ldots,x^{N^b+1}\}$, and their respective masses $\{m^1,\ldots,m^{N^b+1}\}$. $\boldsymbol{x}_i^q$ represents the coordinate vector of node x^q and l^q the distance from x^q to x^{q+1} (with $1\leqslant q\leqslant N^b$). The orientation of an element is defined by $\boldsymbol{t}_i^q$, the unit vector pointing from x^q to x^{q+1}. $\boldsymbol{u}_i^q$ is introduced as obtained by an anticlockwise rotation of $\boldsymbol{t}_i^q$ through 90°. The rotation at node x^q (x^{q+1} in Fig. 4), denoted as δ^q (δ^{q+1}), is defined by the angle between $\boldsymbol{t}_i^q$ and $\boldsymbol{t}_i^{q+1}$.

Motion

Finite-Difference Scheme

In the model, the features that have inertial effects are the lumped masses added to the nodes only. The dynamic laws are applied to them to calculate their motion. Due to the punctual nature of the distribution of mass, the rotation of the nodes has no inertial effects, the translational motion alone can be determined. Actually, it does not restrain any degrees of freedom. The rotation of a spar element is allowed by different translational motions of its nodes.

The position of each node is determined step-by-step at time intervals Δt with a centered finite-difference scheme. Knowing the resultant force vector $\mathbf{R}_i^q$ acting on node x^q, Newton's second law gives its translational acceleration as

$$\ddot{\boldsymbol{x}}_i^q = \boldsymbol{R}_i^q/m^q \tag{7}$$

If the acceleration and velocity are assumed to be constant over a time step, the velocity at $t+\Delta t/2$ is given by Eq. (8), and the position at $t+\Delta t$ by Eq. (9).

$$\lfloor\dot{\boldsymbol{x}}_i^q\rfloor_{t+\Delta t/2} = \lfloor\dot{\boldsymbol{x}}_i^q\rfloor_{t-\Delta t/2} + \lfloor\ddot{\boldsymbol{x}}_i^q\rfloor_t \times \Delta t \tag{8}$$

$$\lfloor\boldsymbol{x}_i^q\rfloor_{t+\Delta t} = \lfloor\boldsymbol{x}_i^q\rfloor_t + \lfloor\dot{\boldsymbol{x}}_i^q\rfloor_{t+\Delta t/2} \times \Delta t \tag{9}$$

Damping

If the behavior is assumed to be of the elastic type, the energy supplied to the inclusion may not dissipate. Therefore damping the equations of motion may be necessary in some cases to arrive at a static or steady state solution. The local nonviscous damping proposed for spar elements is similar to the one described in Cundall (1987). A damping force term is introduced in Eq. (7) via the dimensionless coefficient of damping χ. The damped acceleration in direction i is calculated in Eq. (10), where χ lies between zero (no damping) and one (no acceleration).

$$\ddot{\boldsymbol{x}}_{(i)}^q = \lfloor\boldsymbol{R}_{(i)}^q - \chi\cdot|\boldsymbol{R}_{(i)}^q|\cdot\mathrm{sgn}(\dot{\boldsymbol{x}}_{(i)}^q)\rfloor/m^q \tag{10}$$

Calculating the Resultant Forces Applied on Nodes

As stated in Fig. 5, several types of loads contribute to the resultant force vector $\boldsymbol{R}_i^q$ acting on node x^q. The contributions due to internal loads will be distinguished from those due to external loads. The internal loads are the axial forces T^{q-1} and T^q in the adjacent elements, the bending moments B_3^{q-1} and B_3^{q+1} at nodes x^{q-1} and x^{q+1}, and the gravitational force. The contributions of those loadings to force vector $\boldsymbol{R}_i^q$ are denoted, respectively $\boldsymbol{R}_i^{q(T)}$, $\boldsymbol{R}_i^{q(M)}$, and $\boldsymbol{R}_i^{q(G)}$. External loads are those generated at the contacts between disks and spar elements. Considering the set $\{y^1,y^2,\ldots,y^{N^c}\}$ of disks in interaction with node x^q, $\boldsymbol{R}_i^{p\to q(C)}$ will denote the contribution to $\boldsymbol{R}_i^q$ that is due to the force $\boldsymbol{f}_i^{p\to q}$ applied by disk y^p (with $1\leqslant p\leqslant N^c$).

The method to calculate the contributions listed above is detailed in this section. Finally, $\boldsymbol{R}_i^q$ will be calculated by summing all terms in Eq. (11).

$$\boldsymbol{R}_i^q = \boldsymbol{R}_i^{q(T)} + \boldsymbol{R}_i^{q(M)} + \boldsymbol{R}_i^{q(G)} + \sum_{p=1}^{p=N^c}\boldsymbol{R}_i^{p\to q(C)} \tag{11}$$

Internal Loads

Axial Load. The axial force in a spar element is calculated from the distance between the nodes, with respect to the constitutive behavior assumed. In the present work, spar elements are considered as tension-only features and a linear relation is assumed between the tension T^q and axial strain ε^q in element b^q. This relation is given in Eq. (12), where J=stiffness of the inclusion. ε^q is obtained as $\ln(l^q/l_0^q)$, where l^q and l_0^q=respectively, the current length and the length at repose of b^q. In Eq. (12), tensile forces are represented by positive values. This relation between T^q and ε^q is not inherent in the method. Reaction to compression, nonlinear stiffness, or different stiffness values in charge and discharge could equally well be assumed.

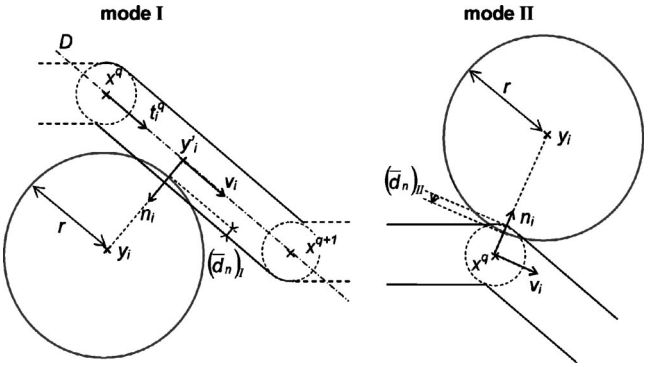

Fig. 6. Definition of the disk-inclusion contacts

$$T^q = \max\lfloor J \cdot \varepsilon^q; 0\rfloor \tag{12}$$

The resultant force vector $\boldsymbol{R}_i^{q(T)}$ acting on node x^q is the sum of the tensile force vectors in elements b^{q-1} and b^q, so that

$$\boldsymbol{R}_i^{q(T)} = T^q \cdot \boldsymbol{t}_i^q - T^{q-1} \cdot \boldsymbol{t}_i^{q-1} \tag{13}$$

Bending Moments. If it were assumed that a bending moment B_3^q is generated by the rotation δ^q at node x^q, then it would result in forces applied on nodes x^{q-1} and x^{q+1}. The relation between δ^q and B_3^q may be defined as in Eq. (14), considering the joints between elements as rotational springs of stiffness k_M^q. To simulate a beam with moment of inertia I and Young's modulus E_y, the equivalent rotational stiffness would be taken equal to $2 \cdot E_y \cdot I/(l_0^{q-1} + l_0^q)$ for node x^q.

$$B_3^q = -\delta^q \cdot k_M^q \tag{14}$$

Finally, considering the bending moments at nodes x^{q-1} and x^{q+1} this time, the resultant force vector acting on node x^q is

$$\boldsymbol{R}_i^{q(M)} = B_3^{q-1} \cdot \boldsymbol{u}_i^{q-1}/l^{q-1} + B_3^{q+1} \cdot \boldsymbol{u}_i^q/l^q \tag{15}$$

Body Forces Body forces, due gravitational acceleration, may be considered. In this case, the gravitational force vector $\boldsymbol{R}_i^{q(G)}$ acting on node x^q is defined in Eq. (16), where m^q is the mass of the node and g_i is the gravitational acceleration vector.

$$\boldsymbol{R}_i^{q(G)} = m^q \cdot \boldsymbol{g}_i \tag{16}$$

External Loads

Detection of the Contacts To calculate external loads, the contacts existing between the disks and the inclusion must be known. It is considered that a contact exists when a disk overlaps a part of the inclusion. In the algorithm, the list of contacts is updated at each calculation cycle. The procedure to test a contact and to calculate the contact force is summarized below, considering a general disk denoted as disk y. r denotes the radius of the disk and $\boldsymbol{y}_i$ the position vector of its center.

Two different types of contacts may exist (see Fig. 6). First, let us consider the contact between disk y and spar element b^q (mode I). Introducing line D which passes through nodes x^q and x^{q+1}, and the coordinates $\boldsymbol{y}'_i$ obtained after an orthogonal projection of $\boldsymbol{y}_i$ on D, the algebraic distance between y and b^q is defined as

$$(\overline{d}_n)_I = |\boldsymbol{y}_i - \boldsymbol{y}'_i| - e/2 - r \tag{17}$$

The disk is considered effectively in contact with b^q if both conditions are verified in the set of equations (18). This being the case, the unit normal of the contact is introduced as the unit vector $\boldsymbol{n}_i$ pointing from $\boldsymbol{y}'_i$ to $\boldsymbol{y}_i$. Vector $\boldsymbol{v}_i$, indicating the tangential direction, is taken as equal to $\boldsymbol{t}_i^q$.

$$0 < \boldsymbol{t}_i^q(\boldsymbol{y}_i - \boldsymbol{x}_i^q) < l^q$$

$$(\overline{d}_n)_I < 0 \tag{18}$$

As shown in Fig. 6, contacts of the second type (mode II) may occur if the distance between the disk and a node is less than $e/2$. This condition is checked for node x^q by calculating the algebraic distance between the disk and the circle of radius $e/2$ centered on x^q as

$$(\overline{d}_n)_{II} = |\boldsymbol{y}_i - \boldsymbol{x}_i^q| - e/2 - r \tag{19}$$

Then, a contact in mode II exists if

$$(\overline{d}_n)_{II} < 0 \tag{20}$$

If so, the unit normal $\boldsymbol{n}_i$ points from $\boldsymbol{x}_i^q$ to $\boldsymbol{y}_i$ and the tangential direction is defined by the unit vector $\boldsymbol{v}_i$, perpendicular to $\boldsymbol{n}_i$ and oriented as the numbering of the elements. Note that both mode I and mode II [i.e., Eqs. (18) and (20)] may be satisfied simultaneously. Mode I is considered by default in that case.

Contact Laws. An expression of the contact force vector $\boldsymbol{f}_i$ applied by the disk on the inclusion is proposed now. It is assumed that before failure, the contact is equivalent to springs in both directions defined in the previous paragraph. k_n and k_t denote, respectively, the normal and the tangential stiffness. The normal component f_n of the contact force is defined in Eq. (21), where $\overline{d_n}$ represents $(\overline{d_n})_I$ or $(\overline{d_n})_{II}$.

$$f_n = \overline{d_n} \cdot k_n \tag{21}$$

The shear component f_t of the shear force is incremented at each time step on the base of the tangential displacement increment $\Delta\overline{d_t}$ at the contact. Assuming that the displacement of the inclusion varies linearly between two nodes, $\Delta\overline{d_t}$ is obtained in Eq. (22) and f_t in Eq. (23).

$$\Delta\overline{d_t} = [(1-\xi)\dot{\boldsymbol{x}}_i^q + \xi \cdot \dot{\boldsymbol{x}}_i^{q+1} - \dot{\boldsymbol{y}}_i - \dot{\theta}_3 \cdot r \cdot \boldsymbol{t}_i^q]\boldsymbol{t}_i^q \times \Delta t$$

$$\xi = \begin{cases} |\boldsymbol{y}'_i - \boldsymbol{x}_i^q|/l^q & \text{for contacts in mode I} \\ 0 & \text{for contacts in mode II} \end{cases} \tag{22}$$

$$\Delta f_t = k_t \cdot \Delta\overline{d_t} \tag{23}$$

The shear strength of the contact is defined by a Coulomb-like slip model with friction angle μ. At each time step, the contact is checked for slip condition by calculating $f_t^{\max}$, the maximum allowable magnitude of f_t, and by comparing it to the sum $f_t + \Delta f_t$. That is done in Eq. (24).

$$(f_t)_{N+1} = \text{sgn}[(f_t)_N + (\Delta f_t)_N] \times \min[(f_t^{\max})_{N+1}; |(f_t)_N + (\Delta f_t)_N|]$$

$$f_t^{\max} = |f_n| \cdot \tan\mu \tag{24}$$

Finally the contact force vector $\boldsymbol{f}_i$ is obtained as

$$\boldsymbol{f}_i = f_n \cdot \boldsymbol{n}_i + f_t \cdot \boldsymbol{v}_i \tag{25}$$

When a slip occurs, it is possible for the disk to change the spar element it is in contact with (or the mode of the contact). That is

accounted for in the algorithm. The shear component of the contact force is not affected (i.e., is not set to zero), $\boldsymbol{n}_i$ and $\boldsymbol{v}_i$ are simply updated with respect to the new configuration of the contact. With this condition, $\boldsymbol{f}_i$ is defined as a continuous function of the relative displacement. Note that the simple laws that describe the constitutive behavior of disk-inclusion contacts are not intrinsic to the method. More complex laws of behavior could replace Eqs. (21) and (23).

Distributing the Contact Forces on the Nodes Considering the contact force f_i applied by the disk in contact with spar element b^q (mode I), it is assumed that the forces acting on nodes x^q and x^{q+1} are as defined in the set of equations (26). These equations are based on the analogy with an elastic beam resting on two supports. They also apply to mode II, ξ is equal to 0 and $\boldsymbol{f}_i$ acts directly on node x^q in that case.

$$\boldsymbol{R}_i^{q(C)} = \boldsymbol{f}_i(1-\xi)$$

$$\boldsymbol{R}_i^{q+1(C)} = \boldsymbol{f}_i \cdot \xi \tag{26}$$

Critical Time Step

The time step has to be less than a critical value for a centered finite-difference scheme to produce a stable solution. The critical time step is related to the minimum eigenperiod of the total system. It is estimated following the same procedure as in Hart et al. (1988).

A value of the critical time step is found for each node x^q by applying Eq. (27) separately to each degrees of freedom and assuming that the degrees of freedom are uncoupled.

$$\Delta t_{\text{crit}}^q = \sqrt{m^q/\overline{K_{(i)}^q}} \tag{27}$$

In Eq. (27), $\overline{K_{(i)}^q}$ is the equivalent translational stiffness in direction i. It is computed as follows. First, consider the relation in Eq. (28) between the force increment vector $\Delta\boldsymbol{R}_i^q$ acting on node x^q and the displacement increment vector $\Delta\boldsymbol{x}_i^q$. In the equations below, the superscript $p \rightarrow q$ denotes variables related to the contact between disk y^p and node x^q.

$$\Delta\boldsymbol{R}_i^q = \Delta\boldsymbol{R}_i^{q(T)} + \Delta\boldsymbol{R}_i^{q(M)} + \Delta\boldsymbol{R}_i^{q(G)} + \sum_{p=1}^{p=N^c} \Delta\boldsymbol{R}_i^{p\rightarrow q(C)} \tag{28}$$

with

$$\Delta\boldsymbol{R}_i^{q(T)} = -J\frac{\Delta\boldsymbol{x}_j^q \cdot \boldsymbol{t}_j^{q-1}}{l^{q-1}}\boldsymbol{t}_i^{q-1} - J\frac{\Delta\boldsymbol{x}_j^q \cdot \boldsymbol{t}_j^q}{l^q}\boldsymbol{t}_i^q$$

$$\Delta\boldsymbol{R}_i^{q(M)} = -\frac{\Delta\boldsymbol{x}_j^q \cdot \boldsymbol{u}_j^{q-1}}{(l^{q-1})^2}k_M^{q-1} \cdot \boldsymbol{u}_i^{q-1} - \frac{\Delta\boldsymbol{x}_j^q \cdot \boldsymbol{u}_j^q}{(l^q)^2}k_M^{q+1} \cdot \boldsymbol{u}_i^q$$

$$\Delta\boldsymbol{R}_i^{q(G)} = 0$$

$$\Delta\boldsymbol{R}_i^{p\rightarrow q(C)} = -(1-\xi^{p\rightarrow q})^2(k_t \cdot \Delta\boldsymbol{x}_j^q \cdot \boldsymbol{v}_j^{p\rightarrow q} \cdot \boldsymbol{v}_i^{p\rightarrow q} + k_n \cdot \Delta\boldsymbol{x}_j^q \cdot \boldsymbol{n}_j^{p\rightarrow q} \cdot \boldsymbol{n}_i^{p\rightarrow q})$$

Next, considering the matrix form (29) of the relation between $\Delta\boldsymbol{R}_i^q$ and $\Delta\boldsymbol{x}_i^q$, the diagonal terms $\boldsymbol{K}_{ii}^q$ of the stiffness matrix are taken as approximations of $\overline{K_{(i)}^q}$ $(i=1,2)$. Expressing $\boldsymbol{K}_{ii}^q$ from Eq. (28), Eq. (30) is obtained for $\boldsymbol{K}_{(i)}^q$.

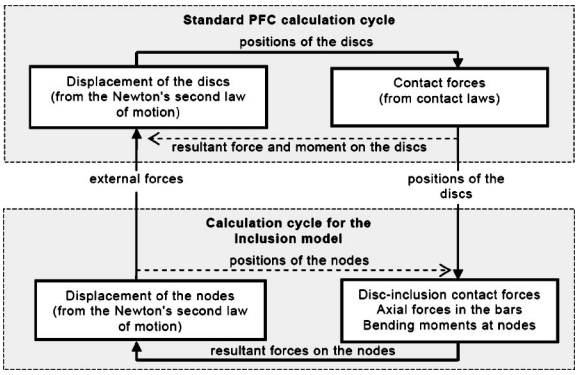

Fig. 7. Coupling a distinct element method code and the distinct spar element method: Calculation cycle

$$\begin{bmatrix}\Delta\boldsymbol{R}_1^q \\ \Delta\boldsymbol{R}_2^q\end{bmatrix} = -\begin{bmatrix}\boldsymbol{K}_{11}^q & \boldsymbol{K}_{12}^q \\ \boldsymbol{K}_{21}^q & \boldsymbol{K}_{22}^q\end{bmatrix}\begin{bmatrix}\Delta\boldsymbol{x}_1^q \\ \Delta\boldsymbol{x}_2^q\end{bmatrix} \tag{29}$$

$$\overline{K_{(i)}^q} = \boldsymbol{K}_{ii}^q = \boldsymbol{K}_{ii}^{q(T)} + \boldsymbol{K}_{ii}^{q(M)} + \sum_{p=1}^{p=N^d} \boldsymbol{K}_{ii}^{p\rightarrow q(C)} \tag{30}$$

where

$$\boldsymbol{K}_{ii}^{q(T)} = J\lfloor(\boldsymbol{t}_{(i)}^{q-1})^2/l^{q-1} + (\boldsymbol{t}_{(i)}^q)^2/l^q\rfloor$$

$$\boldsymbol{K}_{ii}^{q(M)} = k_M^{q-1}(\boldsymbol{u}_{(i)}^{q-1}/l^{q-1})^2 + k_M^{q+1}(\boldsymbol{u}_{(i)}^q/l^q)^2$$

$$\boldsymbol{K}_{ii}^{p\rightarrow q(C)} = (1-\xi^{p\rightarrow q})^2\lfloor k_t(\boldsymbol{v}_{(i)}^{p\rightarrow q})^2 + k_n(\boldsymbol{n}_{(i)}^{p\rightarrow q})^2\rfloor$$

Finally, a value of the critical time step is computed from Eqs. (27) and (30) for each degrees of freedom and for each node. The global critical time step is taken to be the minimum of all values, and the actual time step in the simulation is taken as a fraction of it.

Distinct Element Method–Distinct Spar Element Method Coupling

Basic Concept

The DSEM algorithm has been coupled with the DEM code with the concept of Fig. 7. At the beginning of each time step, the external loads on the inclusion are determined with respect to the positions and velocities of all elements. Next, the motion of DSEM elements is computed from Eq. (10). At this stage, the half-cycle concerning the DSEM is finished. Then, the disk-inclusion contact forces are introduced in the DEM program as a set of forces and moments acting on the disks. This procedure is equivalent to replacing, respectively, Eqs. (1) and (2) by Eqs. (31) and (32). Finally, the positions of the disks are updated for the next calculation cycle.

$$\ddot{\boldsymbol{y}}_i^p = (\mathbf{F}_i^p - \boldsymbol{f}_i^{p\rightarrow q})/m_D^p \tag{31}$$

$$\ddot{\theta}_3^p = (M_3^p - f_t^{p\rightarrow q} \cdot r^p \cdot \boldsymbol{n}_i^{p\rightarrow q} \cdot \boldsymbol{u}_i^q)/I_D^p \tag{32}$$

Critical Time Step

A global value of the critical time step is required for the coupled simulations. In the DEM code, the critical time step associated to

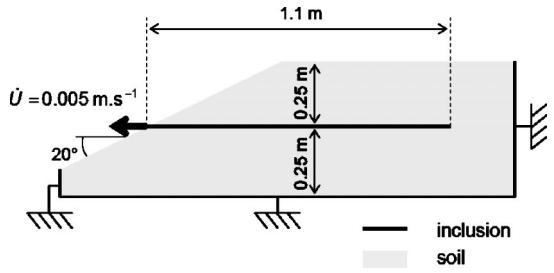

Fig. 8. Geometry and boundary conditions of the pullout test simulated

a disk is estimated on the base of the stiffness of the contacts acting upon it. The procedure, quite similar to that described in the previous section, is detailed in *PFC2D* (1997). By including the stiffness of the disk-inclusion contacts in this procedure, the critical time step related to the disks can be obtained. It is compared to the one related to the DSEM elements, and the minimum of the two is taken as the global critical time step.

Central Processing Unit Time

One of the main advantages of using circular particles in DEM codes is a reduced CPU time. Thus it is not surprising that the Central Processing Unit (CPU) time required for a DSEM element is much more than the one required for a circular particle. In our computations, we found that a DSEM element is equivalent to 10 traditional DEM elements in terms of CPU time. This significant difference has two main origins. The first one, intrinsic in the method, is the more complex shape and constitutive behavior of the DSEM elements. The second one is the spatial search algorithm (based on a cell-space subdivision), probably less optimized in the DSEM than in the commercial DEM code used. This disadvantage has not been considered a major issue, however. In most applications, the number of DSEM elements should be low compared with the number of DEM elements, so that the computing of DSEM elements represents a minor part of the global CPU time.

Simulating Pullout Tests with Two Models for the Inclusion

The results obtained by simulating pullout tests on straight anchorages are reported in this section. They are part of a more general study on geosynthetic anchorages in soil [see Chareyre et al. (2002)]. An inclusion without bending strength was included in a breakable random packing whose geometry and boundary conditions are defined in Fig. 8. The tensile stiffness J of the inclusion was set to 10^3 kN m^{-1}. The inclusion was simulated alternatively with disks or with spar elements to provide a comparison.

Table 1. Definition of the Clusters Used for the Soil Model

	Radius of the disks in the cluster	
Number of clusters	Disk 1 (mm)	Disk 2 (mm)
400	11.60	10.44
1,600	5.80	5.22

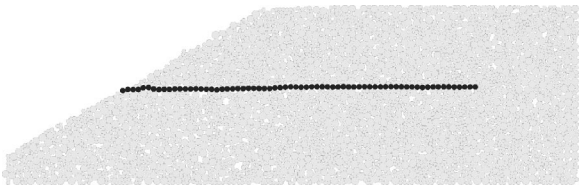

Fig. 9. Initial state of the anchorage in the full-distinct element method simulation

Procedure

In the modeling, the soil was simulated as a random packing of clusters, each cluster being made of two disks connected in a rigid manner (their radii are defined in Table 1). The assembly was generated with an initial porosity equal to 0.2. The density of the clusters was set to 20 kN m^{-2}, the angle of friction between the clusters was set to 38.7°, the normal stiffness k_n^* was set to 5×10^4 kN m^{-1}, and the tangential stiffness k_s^* was set to 2.5×10^4 kN m^{-1}. The macroscopic angle of friction φ_s of such assembly has been estimated by simulating biaxial compressions, and it was found equal to 41° (±0.5°). The method to determine φ_s is detailed in Chareyre and Villard (2002).

The soil mass was set in place between three rigid walls, as in Fig. 8, and submitted to gravitational acceleration. The properties of the cluster-wall contacts were the same as those defined in the previous paragraph. Pullout tests were simulated with a constant velocity, which must be low enough in order to avoid dynamic effects. It was set to 0.002 m/s after several trials.

During the pullout process, the soil above the inclusion applies a vertical load only, and the resistance to pullout is provided by the interaction at the lower soil-inclusion interface. This interaction is represented by two forces Q_n and Q_t, calculated by summing, respectively, the normal components and the tangential components of the contact forces along the lower side of the inclusion. Here "normal" and "tangential" refer to the local orientation of the inclusion. The mobilized angle of macroscopic friction φ_m is defined as $\arctan(Q_t/Q_n)$. In the following, the results will be presented in terms of the evolution of φ_m during the pullout simulations for different values of the angle μ of contact friction at the interface.

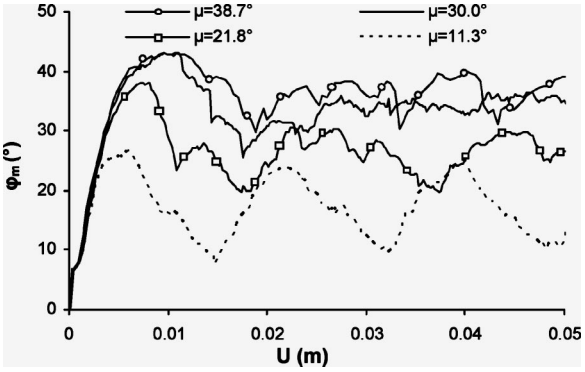

Fig. 10. Evolution of the angle of mobilized friction as a function of the displacement and the angle of contact friction at the interface

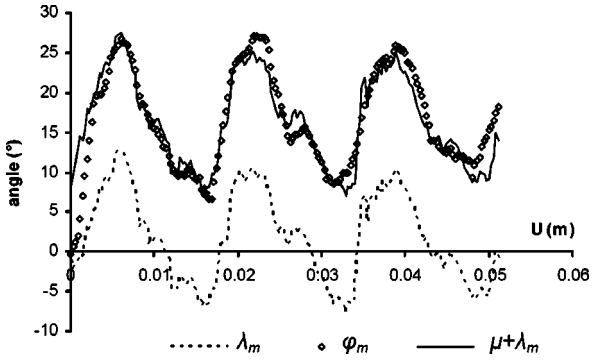

Fig. 11. Comparison between the mean angle of inclination of the contacts' normal and the mobilized friction angle

Results

Full-Distinct Element Method Simulations

Fig. 9 represents the initial state of the model when the inclusion was simulated using a set of 68 disks of radius 8.15 mm. Approximately 2,000 clusters were used to simulate the soil, as defined in Table 1.

The evolution of φ_m is reported in Fig. 10 with respect to the pullout displacement U and the angle of contact friction μ. The initial value of φ_m is close to zero. It rises gradually until it reaches a peak, followed by a strain softening transition. The angle of peak friction depends on μ, the higher it is set, and the higher φ_m is obtained at peak.

After the peak, some important fluctuations of φ_m are noticeable. With the lower values of μ, in particular with $\mu=11.3°$, those fluctuations seem to have a period equivalent to the diameter of the disks simulating the inclusion. For a better understanding of this feature, the orientation of the soil-inclusion contacts along the lower interface was analyzed. The results obtained for the case $\mu=11.3°$ are presented in Fig. 11. Let us consider all the contacts between the lower side of the inclusion and the soil. λ_m is introduced as the mean inclination of the contact normals with respect to the vertical ($\lambda_m>0$ for a clockwise inclination). In Fig. 11, the evolution of λ_m highlights a collective behavior of the contacts, with the same periodicity as φ_m. Moreover, φ_m appears to be very close to $\lambda_m+\mu$, thus demonstrating the role of the collective evolution in the fluctuations of φ_m.

It is suggested that when the model is generated, the cluster assembly representing the soil tends to fit into the periodic roughness of the inclusion. A mechanism similar to that of Fig. 12 (but with a random packing) is enabled then. Note that the tensile stiffness of inclusion was high compared to the load applied, and that its tensile strain was always less than 0.2%. A more deformable inclusion would probably prevent any global periodicity since the disks of the inclusion could not move simultaneously.

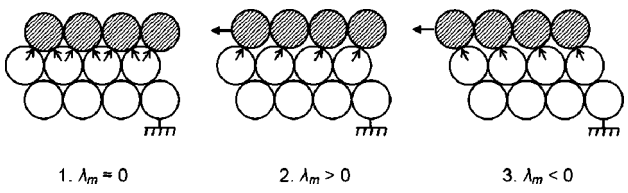

Fig. 12. Principle of the periodic evolution of the contacts at the soil-inclusion interface

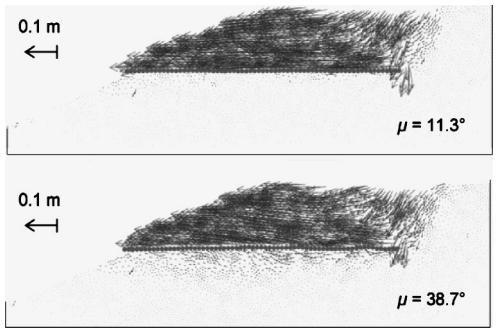

Fig. 13. Displacement of the disks for U from 0 to 0.05 m

No periodic variation in φ_m is noticeable with $\mu=30°$ and $\mu=38.7°$. As seen in Fig. 13, a high value of μ produces displacements of soil elements below the inclusion. It denotes a shear failure within the granular assembly. That is why the periodicity vanishes in that case. Indeed, shearing the random packing of soil elements cannot generate any periodic mechanism.

Coupled Distinct Element Method-Distinct Spar Element Method Simulations

The results obtained by modeling the inclusion with spar elements are presented in this section (the soil being modeled exactly in the same way). Note that, in this problem, it was not necessary to damp the equations of motion for the DSEM elements. A sufficient damping is provided by the friction between the inclusion and the surrounding elements. Fig. 14 demonstrates that the coefficient of damping has no influence on the results in that case.

Fig. 15 shows the evolution of φ_m in the coupled simulation for different values of μ. There is no strain softening. When $\mu\leqslant 30°$, the curves show a gradual increase in φ_m until a constant residual value (however, φ_m drops sporadically during the residual phase). With $\mu\geqslant 38.7°$, φ_m fluctuates during the residual phase. Nevertheless, the fluctuations are smaller than those obtained with the previous modeling, and φ_m can be considered almost constant.

As seen in Fig. 16, the occurrence of fluctuations with the highest values of μ is correlated with a shear deformation of the

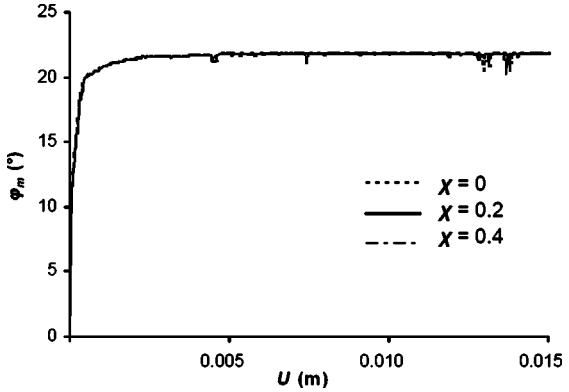

Fig. 14. Evolution of the mobilized angle of friction in the distinct element method-distinct spar element method coupling with $\mu=21.8°$ for different values of the damping coefficient

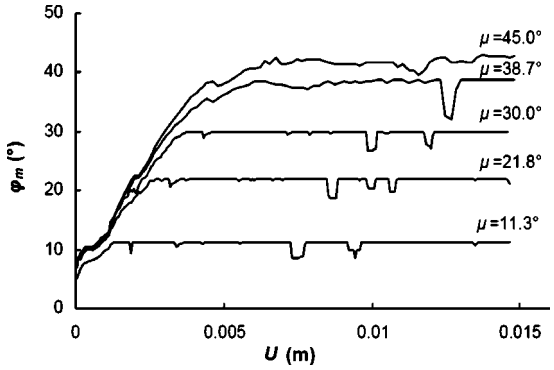

Fig. 15. Evolution of the mobilized angle of friction in the distinct element method-distinct spar element method coupling as function of the displacement and the interface contact friction

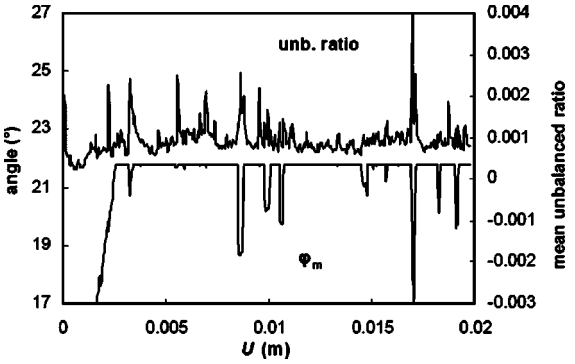

Fig. 17. Comparison between the evolution of φ_m and the evolution of the mean unbalanced force

soil below the inclusion. Note that there are some failures in the soil when $\mu=38.7°$, although the angle of internal friction is higher than μ ($\varphi_s=41°$). In fact, φ_s is a mean macroscopic value and does not represent the effective strength at the granular scale. The interaction with the inclusion can then cause the instability of soft spots in the microstructure, particularly if μ is inferior but close to φ_s.

In order to understand the origin of the temporary diminution of φ_m when $\mu=11.3-30°$, the mean unbalanced ratio (m.u.r.) was compared to φ_m. The m.u.r. is computed on the disks as the mean magnitude of the resultant force [F_i in Eq. (1)] divided by the mean magnitude of the contact forces. It tends to zero when the evolution of the system is quas-istatic. As seen in Fig. 17 for the case $\mu=21.8°$, the decreases in φ_m are correlated with some peaks of the m.u.r. These peaks denote small dynamic events related to contact failures in the soil. It shows that the drops in φ_m are due to local reorganizations of the disks near the interface. φ_m quickly increases back to μ as soon as the disks stabilize.

Macroscopic Versus Microscopic Peak Friction

The maximum value φ_{max} of φ_m (considered as the macroscopic friction angle) is plotted as function of the angle of local friction μ in Fig. 18. The micro–macro relation between μ and φ_{max} is highly dependent on the model used. With the DSEM, there is a very good equivalence between the microscopic and the macroscopic scale, except for $\mu=45°$. With the full-DEM model, the micro-macro relation is more complex. The roughness of the interface causes an increase in the global friction, and this increase depends on μ.

Fig. 17 shows with both the DEM and the DSEM that φ_{max} cannot exceed a maximum value, which is slightly higher than φ_s (angle of internal friction of the soil). A maximum value equal to φ_s could have been expected. But actually, when a shear band of finite thickness develops in the soil below the inclusion, the vertical stress at the depth of the sheared zone is higher than the normal stress at the soil-inclusion interface. The shear strength of the soil at the interface is increased then, and the angle of mobilized friction can slightly exceed φ_s.

Conclusions

A numerical model named DSEM has been proposed to simulate the deformation of a stressed inclusion in two dimensions and its interaction with a granular matter. With the concepts of the DSEM and DEM algorithms being very similar, it was possible to couple the DSEM with the distinct element code *PFC2D*, thus enabling us to simulate the soil-inclusion interaction in composite systems.

Pullout tests on straight anchorages were simulated. Some results obtained with the coupled DEM-DSEM model have been reported and compared with the results of a previous modeling, based on the DEM only, where the inclusion was simulated by a chain of disks. The main difference between those two types of modeling was the shape of the interface between the soil and

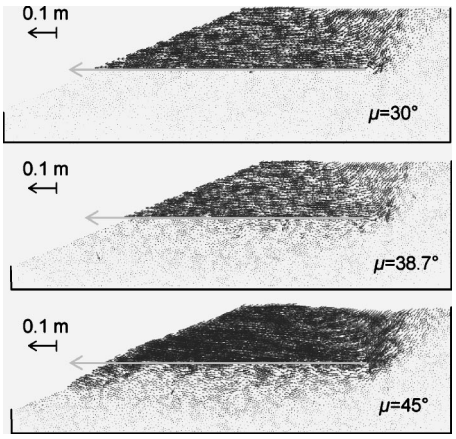

Fig. 16. Displacement of the disks for U from 0 to 0.02 m

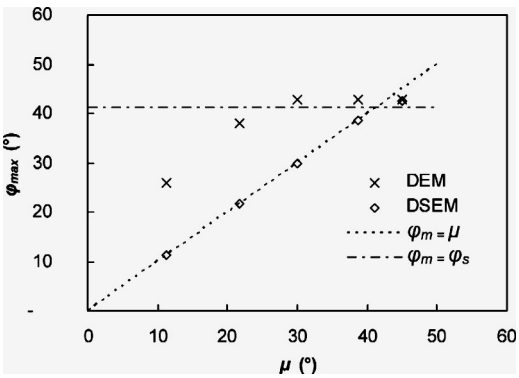

Fig. 18. Global versus local friction angle at the soil-inclusion interface

inclusion, which was locally even in the first case and periodically rough in the second. Whatever the method of modeling is, the soil and the inclusion can interact with two different mechanisms, depending on the local friction angle μ at the interface. When μ is low, the inclusion is pulled-out without notable deformation in the soil. When μ is high enough, a shear band parallel to the geosynthetic develops in the soil. Considering those two mechanisms, only the calculations with the DSEM can provide in both cases some realistic results in terms of global friction. Indeed, when μ is low and the inclusion simulated by disks, the interface roughness generates undesirable periodic oscillations of high magnitude in the global friction.

In case the inclusion is rough (which is generally the case), the DSEM is probably not well suited to study micromechanically the soil-inclusion interaction. However, coupled DEM-DSEM models could be appropriate when the global behavior of composite structures is to be studied. In this case, the effect of the actual roughness may be taken into account globally in the value of μ. In the coupled model, the angles of local and global interface friction are almost equal. This is an important advantage of DSEM compared to DEM. If the global behavior of a soil-inclusion structure is to be simulated, the value of μ in the model can be set directly from macroscopic measurements alone (e.g., μ can be taken equal to the angle of macroscopic friction obtained from shear tests on soil-geosynthetic interfaces). This approach has been used to simulate geosynthetic anchorages with complex shapes. The results are consistent with experimental data, and practical conclusions for design can be drawn from them. Those results will be reported in a future paper.

The concept of the DSEM can be extended to three-dimensional problems by considering a three-dimensional loading on each element. Coupling the DEM and the DSEM in 3D would enable a micromechanical approach for studying different soil reinforcement techniques (fibers, mesh elements, geogrids).

Notation

The following symbols are used in this paper:

B_3 = bending moment at a node;
b = label of a bar;
D = axis of spar element;
$\overline{d}$ = displacement at contact;
e = thickness of the inclusion;
E_y = Young modulus;
$\boldsymbol{F}_i$ = resultant force vector acting on a disk;
$\boldsymbol{f}_i$ = disk-inclusion contact force;
$f_t^{\max}$ = threshold value of the shear force at contact;
$\boldsymbol{g}_i$ = gravitational acceleration vector;
I_D = moment of inertia of disk y^n;
I = moment of inertia of a beam;
J = axial stiffness of the inclusion;
$\overline{K}$ = translational stiffness;
K_{ij} = terms of the stiffness matrix;
k_n = normal stiffness at disk–inclusion contacts;
k_n^* = normal stiffness at disk–disk contacts;
k_t = tangential stiffness at disk–inclusion contacts;
k_t^* = tangential stiffness at disk-disk contacts;
k_M = rotational stiffness of a node;
l = length of a spar element;
l_0 = length at repose of a spar element;
M_3 = resultant moment acting on a disk;
m = mass of a node;
m_D = mass of a disk;
N^b = number of spar elements;
N^c = number of disks interacting with a node;
n_i = unit normal of the current contact;
$\boldsymbol{Q}$ = force of lower interface interaction;
$\boldsymbol{R}_i$ = resultant force vector acting on a node;
r = radius of a disk;
t = time;
T = axial load;
$\boldsymbol{t}_i$ = unit vector parallel to D;
U = pullout displacement;
$\boldsymbol{u}_i$ = unit vector perpendicular to D;
$\boldsymbol{v}_i$ = unit tangent of a contact;
$\boldsymbol{x}_i$ = position vector of a node;
x = label of a node;
$\boldsymbol{y}_i$ = position vector of the center of a disk;
y = label of a disk;
$\boldsymbol{y}_i'$ = orthogonal projection of y_i on D;
Δt_{crit} = critical time step;
δ^n = angle of deflection at node x^n;
ε^n = axial strain in element b^n;
θ_3 = angle of rotation of a disk;
λ_m = mean angle of inclination of the interface contact normals;
μ = friction angle at disk–inclusion contacts;
μ^* = friction angle at disk-disk contacts;
ξ = factor of influence of a contact;
φ_s = internal friction angle of the disk assembly;
φ_m = angle of mobilized interface friction;
$\varphi_{\max}$ = angle of peak interface friction; and
χ = coefficient of damping.

Subscripts

i, j = integer indices equal to 1 or 2;
n = normal component; and
t = tangential component.

Superscripts

C = related to contact forces;
G = related to gravitational forces;
M = related to bending moments;
p, q = positive integer exponents; and
T = related to tensile loads.

References

Chareyre, B., Briancon, L., and Villard, P. (2002). "Theoretical versus experimental modeling of the anchorage capacity of geotextiles in trenches." *Geosynthet. Int.*, 9(2), 97–123.

Chareyre, B., and Villard, P. (2002). "Discrete element modeling of curved geosynthetic anchorages with known macro-properties." *Proc., First Int. PFC Symposium*, Gelsenkirchen, Germany, 197–203.

Cundall, P. A. (1987). "Distinct element model of rock and soil structure." *Analytical and computational methods in engineering rock mechanics*, E. T. Brown, ed., Allen & Unwin, London, 129–163.

Cundall, P. A., and Strack, O. D. L. (1979). "A discrete numerical model for granular assemblies." *Geotechnique*, 29(1), 47–65.

Hart, R., Cundall, P. A., and Lemos, J. (1988). "Formulation of a three-dimensional distinct element model. II: Mechanical calculations for motion and interaction of a system composed of many polyhedral blocks." *Int. J. Rock Mech. Min. Sci. Geomech. Abstr.*, 25(3), 117–125.

Hentz, S., Daudeville, L., and Donze, F. (2003). "Modeling of reinforced concrete structures subjected to impacts by the discrete element method." *Proc., 16th Engineering Mechanics Conf.*, EM2003, ASCE, Reston, Va.

Mohammadi, S., Owen, D. R. J., and Peric, D. (1998). "A combined finite/discrete element algorithm for delamination analysis of composites." *Finite Elem. Anal. Design*, 28(4), 321–336.

PFC2D user manual; release 1.10. (1997). Itasca Consulting Group, Inc., Minneapolis.

Villard, P., Kotake, N., and Otani, J. (2002). "Modeling of reinforced soil in finite element analysis." Keynote lecture, *Proc., 7th Int. Conf. on Geosynthetics*, J. P. Gourc and P. Delmas, eds., Nice, France, 39–95.